RESEARCH ARTICLE

WILEY

Internal structure and palsa development at Orravatnsrústir Palsa Site (Central Iceland), investigated by means of integrated resistivity and ground-penetrating radar methods

Adrian Emmert [ID] | Christof Kneisel [ID]

Institute of Geography and Geology, University of Würzburg, Germany

Correspondence
Christof Kneisel, Institute of Geography and Geology, University of Würzburg, D-97074, Germany.
Email: kneisel@uni-wuerzburg.de

Abstract

The natural cyclical development of palsas makes it difficult to use visible signs of decay as reference points for environmental change. Thus, to determine the actual development stage of a palsa, investigations of the internal structure are crucial. Our study presents 2-D and 3-D electrical resistivity imaging (ERI) and 2-D ground-penetrating radar (GPR) results, measurements of surface and subsurface temperatures, and of the soil matric potential from Orravatnsrústir Palsa Site in Central Iceland. By a joint interpretation of the results, we deduce the internal structure (i.e., thickness of thaw zone and permafrost, ice/water content) of five palsas of different size and shape. The results differentiate between initial and mature development stages and show that palsas of different development stages can exist in close proximity. While internal characteristics indicate undisturbed development of four palsas, one palsa shows indications of environmental change. Our study shows the value of the multimethod geophysical approach and introduces measurements of the soil matric potential as a promising method to assess the current state of the subsurface.

KEYWORDS
3-D electrical resistivity imaging, ground-penetrating radar, palsa development, soil matric potential

1 | INTRODUCTION

Palsas undergo cyclical formation and decay, controlled by complex interactions between environmental factors such as surface and subsurface temperatures, the occurrence of insulating snow cover, and the availability of liquid water.[1] These factors are changing fundamentally in Arctic and Subarctic environments today,[2] and palsas may provide a critical record of this change, if the complexities associated with their formation and degradation can be untangled. This is particularly important, considering that studies report a strong loss of palsa landscapes in several regions.[3,4] Evaluating the impact of climate warming to palsas is difficult, as the complex energy fluxes between the surface and the subsurface are not fully understood yet.[5] However, insights into their internal structure can provide valuable information on palsa development and serve as an archive of past environmental conditions.[6,7]

Numerous studies have focussed on the vegetation patterns and soil layering surrounding palsas, as well as dating approaches based on plant macrofossils or tephra layers.[8–12] Regarding investigations of the internal structure, nondestructive geophysical techniques such as

electrical resistivity imaging (ERI) or ground-penetrating radar (GPR) are frequently performed.[6,13] The application of ERI has proven its strength particularly for assessing ice content variations and for estimating the depth of the frozen layer.[7,14–17] The main targets for GPR surveying are assessments of the shape of the frozen core and the thickness of seasonal thaw or the active layer.[18,19] To benefit from the advantages of both methods, joint applications can be performed.[20] Combined with information on palsa heights, knowledge of the subsurface layering obtained helps to assess the ratio between permafrost thickness and palsa uplift, which can be used to determine the current development stage of a palsa.[21,22]

The results of case studies from different areas agree on the occurrence of small-scale variations between frozen and unfrozen subsurface conditions and highlight a high spatial variability of active layer thickness.[10,12–14] Previous research at the Orravatnsrústir Palsa Site in Iceland shows an increasing active layer thickness from 0.69 m in 2004 to 0.81 m in 2010 at one specific palsa,[23] and results from another study[16] show that the average active layer thickness increased from between 0.45 and 0.65 m in 2001 to between 0.77 and 0.81 m in 2006.

The objective of the present study is to assess the spatial distribution of ground ice, the magnitude of subsurface ice content variations, and the frost table topography at Orravatnsrústir Palsa Site, which are then used to deduce the current development stages of individual palsas. We use two geophysical techniques and recorded values of temperature and soil matric potential. As the investigated landform units lack large amounts of peat, probably because the organic content has been lowered by steady eolian deposition,[23] they could also be described by the term "lithalsa."[24] However, we use the term "palsa" in this study to keep consistency with the nomenclature of prior studies from Orravatnsrústir.

2 | STUDY SITE

Orravatnsrústir Palsa Site (65.08°N, 18.53°W, Figure 1a) is located in the uninhabited and mostly barren desert of central Iceland, 14 km north of Hofsjökull glacier. Detailed weather data are not available from the area, but data from weather station Hveravellir (55 km away) show a cold tundra climate and relatively low precipitation, particularly in summer, of around 705 mm/a[23] (see Figure 1b). The study site is located in a zone of basic and intermediate interglacial and supraglacial lavas with intercalated sediments that are younger than 0.8 million years.[25] In contrast to the surrounding barren desert, the
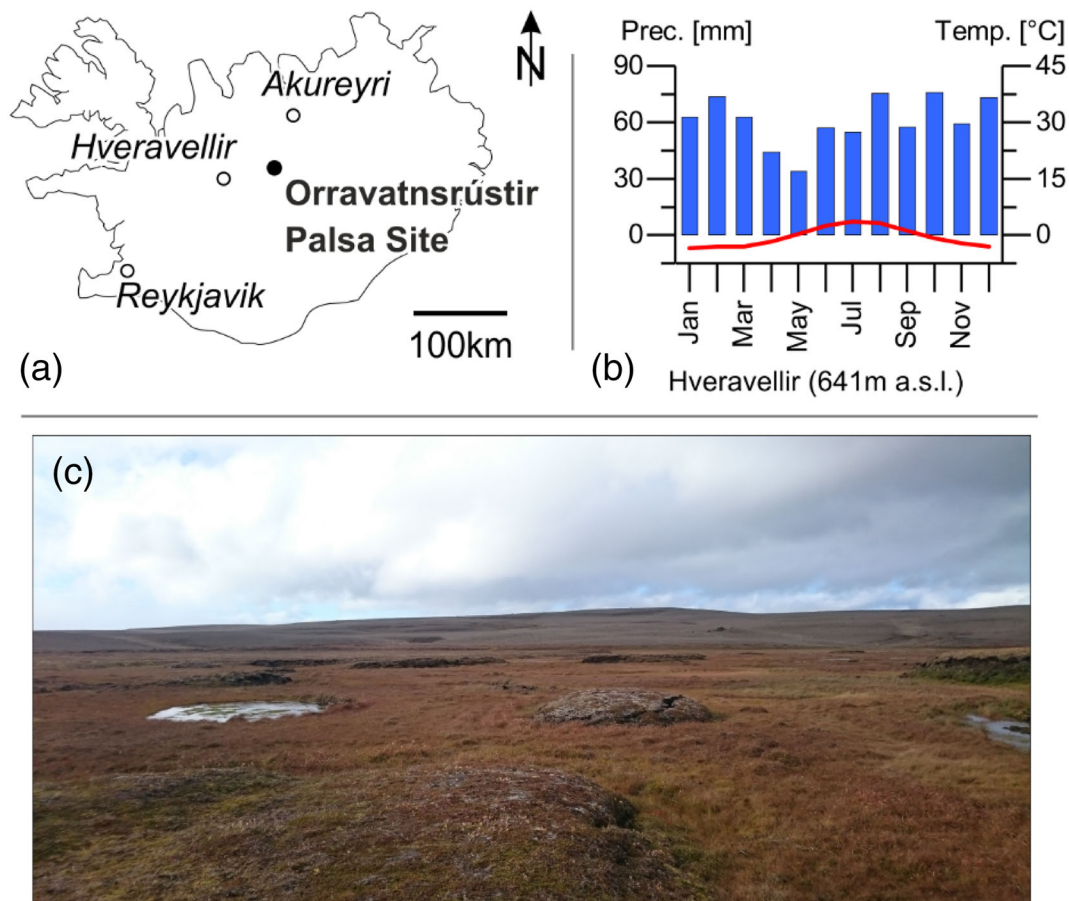

FIGURE 1 Site overview. (a) Map, (b) climate data from nearest weather station Hveravellir (55 km away), and (c) overview photo (picture date: September 20, 2015)

wetland is densely vegetated with mosses and dwarf shrubs on the palsas and with sedges and grasses in their surroundings (Figure 1c).

The formation of ground ice in the region surrounding Lake Orravatn started after 4,500 years before today, and the formation of palsas is still ongoing.[7,8] Previous evidence suggests that the depth to the bottom of permafrost is between 5 and 7.5 m and that mean annual ground surface temperature (MAGST) was 1.0°C between July 2006 and July 2007.[7] The curve of daily mean temperature values from the same time span indicates the absence of thick snow cover on the palsas.[7]

Among the numerous palsas at the Orravatnsrústir Palsa Site, five palsas were investigated in detail for this study (Figures 1c and 2, Table 1). These comprise smaller landform units within the wetland (OVR01, OVR02, OVR05) and larger landform units surrounded by open water (OVR03, OVR04). An aerial picture from 1998 indicates that the palsas OVR03 and OVR04 are remnants of one large palsa or one palsa plateau.[23] Ongoing degradation was visually observed by the authors in the field by an enlargement of the gap between OVR03 and OVR04 (see Figure 2c) between 2015 and 2017.

3 | METHODS

The application of geophysical methods is well established in permafrost research,[26] and the general principles are hence only briefly summarized here.

3.1 | Electrical resistivity imaging (ERI)

ERI characterizes subsurface differences in electrical properties of different earth materials.[27] In permafrost-related studies, this enables ERI to distinguish frozen from unfrozen materials by a high-resistivity contrast caused by the poor electrolytic propagation of electric current in frozen materials.[28]

Two different ERI approaches were used in this study. While electrodes were set up along a linear profile line for the traditional 2-D ERI approach, the 3-D approach of our study uses a rectangular grid of electrodes for data acquisition. This approach enables the measurement of diagonal quadripoles and provides a higher density of data points, compared to merging data from intersecting 2-D surveys only. We used a Syscal Pro Resistivity Meter for data acquisition and the software packages RES2DINVx64 (Ver. 4.05.32, Geotomo Software) and RES3DINVx64 (Ver. 3.11.57, Geotomo Software), respectively, for data processing. Measurements were performed with the Wenner–Schlumberger electrode configuration, but at some locations, additional dipole–dipole surveys were also performed. The resulting data sets were compared (see Figure 3a,b as examples) and the data points from both surveys were merged into one data set to benefit from the advantages of both configurations. These are, for example, penetration depth (better with Wenner–Schlumberger) or horizontal resolution (better with dipole–dipole).[27,28]

Data processing included an elimination of bad data points caused by high contact resistance values and a trial inversion to filter outliers.
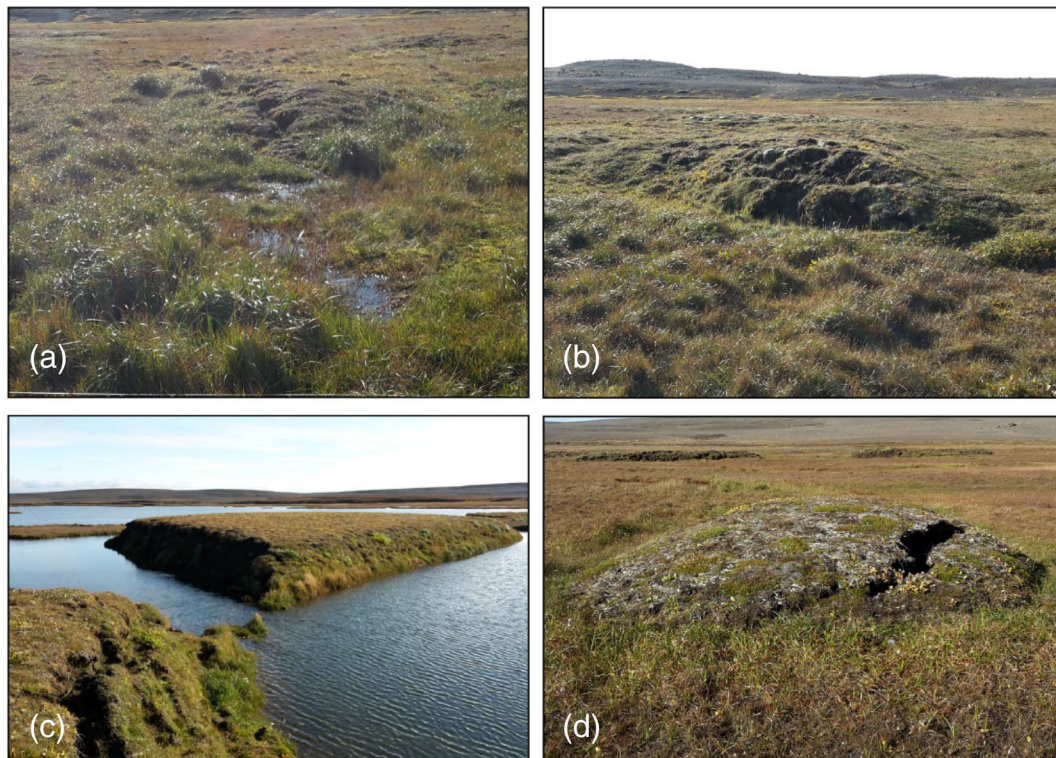

FIGURE 2 Photo compilation of investigated palsas. (a) OVR01, (b) OVR02, (c) OVR04 (front) and OVR03 (back), and (d) OVR05. Date of all pictures: September 9, 2017

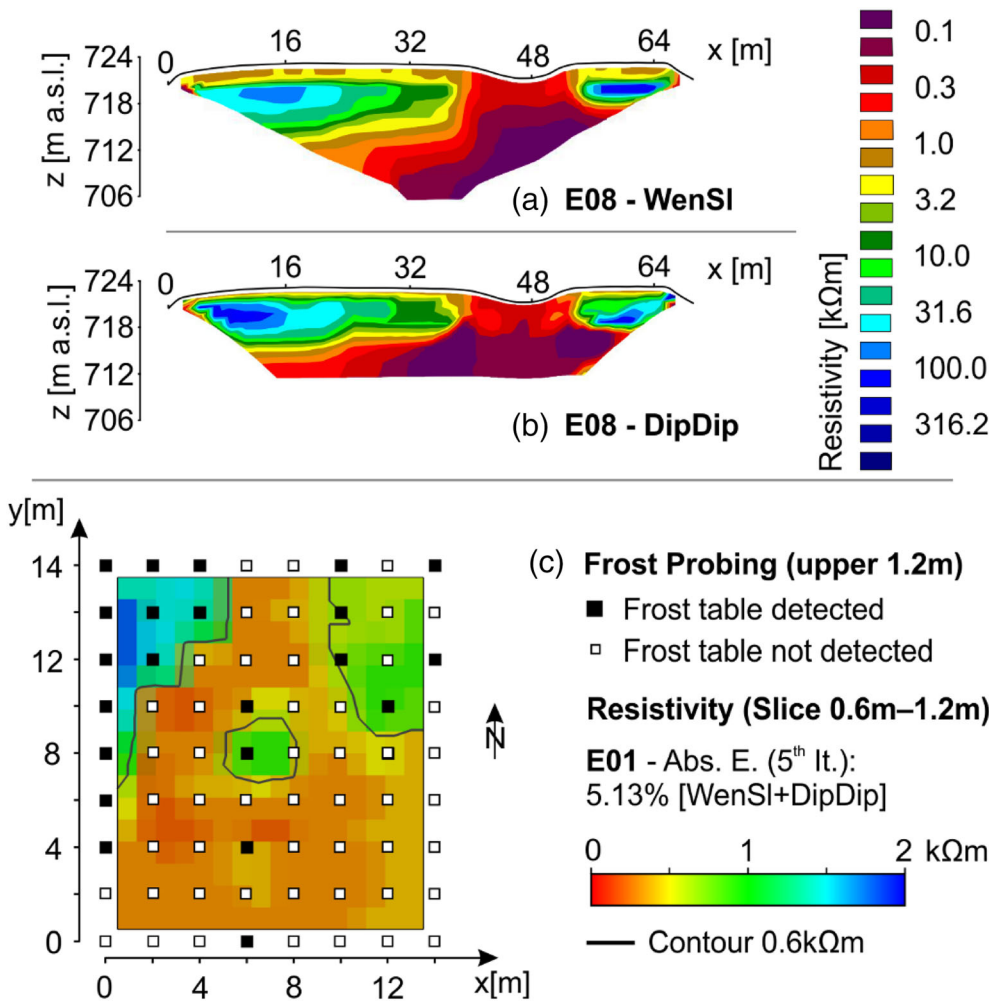| Label	Max. height (m)	Extent of uplifted area (m^2)	Comment
OVR01	0.5	30	Shallow water logs
OVR02	1	240	Uplifted area
OVR03	2.4	1,090	Part of plateau
OVR04	2.4	1,400	Part of plateau, surface cracks
OVR05	1	40	Surface crack

FIGURE 3 Example ERI 2-D and 3-D profiles. (a,b) Visual comparison between models from WenSl and DipDip surveying. Data from E08. (c) Determination of threshold between frozen and unfrozen materials by a comparison between a 3-D ERI model slice of E01 and results from manual frost probing. Boundary reflects the 0.6-kΩm isotherm

To ensure comparability between results, the same inversion parameters (e.g., damping factors, filters, number of nodes) were used for all data sets. We used the robust inversion method (L1-norm), which tries to reduce the absolute difference between the measured and the calculated apparent resistivity, because the appearance of single outlying data points, such as caused by an insufficient ground coupling, was expected in the rough environment. Consequently, error values of the results are presented as "absolute error" values. The inversion process was stopped after the decrease of this error measure leveled out, which happened after the fifth iteration step.

To evaluate if a resistivity model is sufficiently resolved, a resolution matrix approach was used.[29–32] This approach estimates the information content of each model cell and provides a measure on the influence of the inversion settings and of neighboring model cells. Parts of the models with relatively low values were hence interpreted particularly carefully. To estimate a local threshold between frozen and unfrozen materials, we compared the upper model slice of the E01 model (depth level: 0.6–1.2 m) with results from frost-probing with a 1.2-m-long steel rod, which was performed on the same day (see Figure 3c). The comparison shows that a maximum alignment is achieved by a threshold value of 0.6 kΩm. Thus, resistivity values above this threshold are referred to as "high resistivity values" in the following sections, while values below are referred to as "low resistivity values." Seven 2-D ERI surveys and three 3-D ERI surveys were performed (see Tables 2 and 3 for details and Figure 4 for locations).

TABLE 2 Details of 3-D ERI surveys. WenSl = Wenner–Schlumberger, DipDip = dipole–dipole

Survey	Array type	Survey area (m²)	Electrode spacing (m)	Survey date
E01	WenSl+DipDip	56	1	Sep 17, 2015
E02	WenSl+DipDip	56	1	Sep 20, 2015
E07	WenSl+DipDip	56	1	Sep 16, 2015

TABLE 3 Details of 2-D ERI surveys. WenSl = Wenner–Schlumberger, DipDip = dipole–dipole

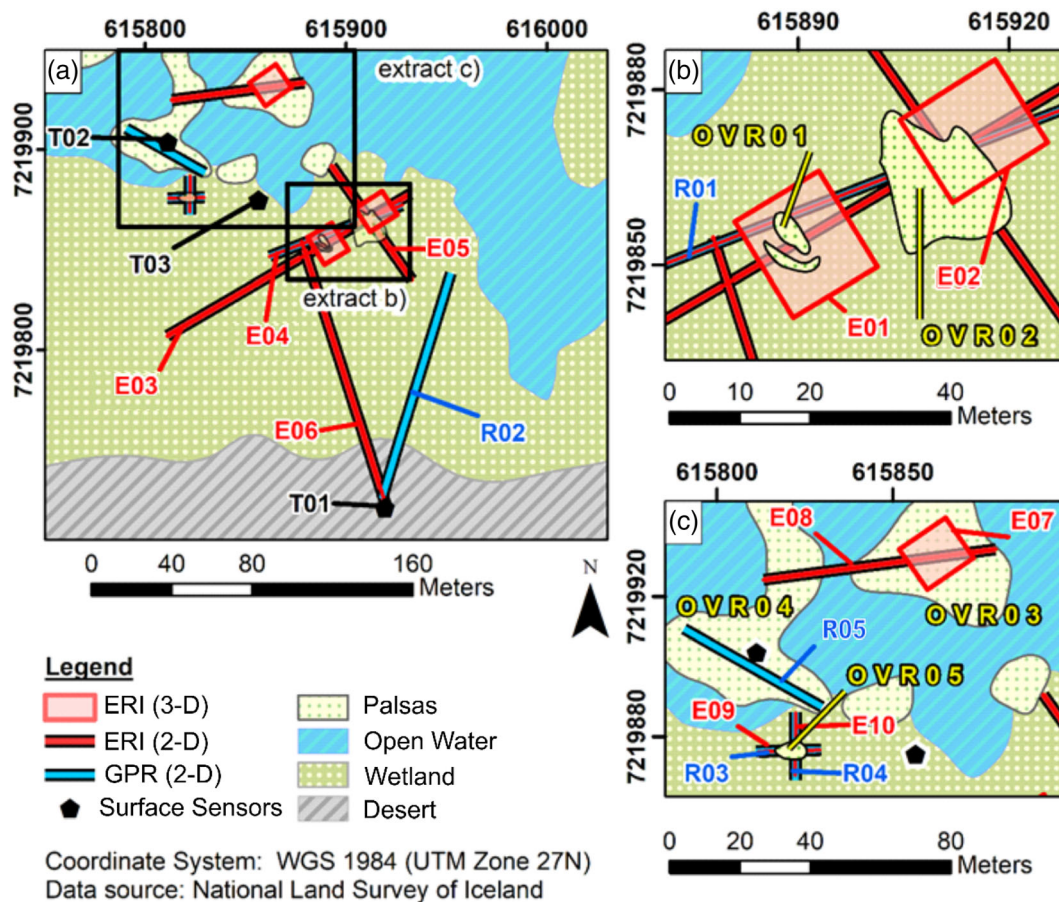| Survey	Array type	Survey length (m)	Electrode spacing (m)	Survey date
E03	WenSl	142	2	Sep 17, 2015
E04	WenSl	71	1	Sep 6, 2017
E05	WenSl	70	2	Sep 20, 2015
E06	WenSl+DipDip	142	2	Sep 20, 2015

FIGURE 4 Map of survey locations (own drawing, based on GNSS surveying). Only selected palsas are displayed

3.2 | Ground-penetrating radar (GPR)

GPR characterizes subsurface structures based on the reflection of artificially created electromagnetic (EM) waves responding to layers with different electrical properties.[33] In permafrost, an electric contrast generally occurs between thawed ground or the active layer and permafrost. This is because the physical properties of liquid water (which occurs in a greater percentage in thawed ground) and ice differ strongly.[34] GPR also assists with distinguishing between

different types of material and deposition process.[33] Herein, we characterize and interpret reflection patterns or so-called "radar facies."[35] We further use reflection triplet sequences for interpretation.[36] These triplet sequences result from differences in dielectric contrasts at reflector boundaries. If the deeper layer at such a boundary has a higher relative permittivity (e.g., at the interface between an upper layer of unsaturated sediments and a deeper layer of saturated sediments), a positive triplet appears. If the upper layer has a higher permittivity (e.g., at the interface between an

upper layer of saturated sediments and the permafrost table below), a negative triplet appears.[36]

We used a PulseEKKO Pro System with unshielded antennas in bistatic data acquisition mode and the software package ReflexW (Sandmeier geophysical research, Ver. 8.5.3) for data analysis (see Table 4 for profile details). Data processing included dewow filtering, time-zero correction and time-depth conversion. For this step, we manually developed 2-D EM-wave velocity models with values based on literature from other palsa and lithalsa sites[18,20,37–39]: at positions of the radargram that correspond to palsa locations, the model consists of two layers—the unfrozen upper subsurface of the palsas is represented by an EM-wave velocity of 0.05 m/ns, while the frozen core below is represented by a value of 0.16 m/ns, reflecting a relatively high ice content. The depth of the boundary between these two model layers was set to the depth of the frost table, as determined by frost-probing. At survey positions between the palsas, where we did not reach the frost table by frost-probing, an EM-wave velocity value of 0.036 m/ns is used throughout the model depth, representing the high degree of water-saturation indicated by the results from measuring the soil matric potential.

While we used results from frost-probing to calibrate the upper layer, the other parts of the models could not be calibrated, due to the absence of diffraction hyperbolas and Common Mid-Point (CMP) surveys. Since we cannot provide values of ice content, inaccuracies in depth assignments in the subsurface below the frost table must be considered. Five GPR profiles were collected (see Table 4 for details and Figure 4 for locations). Roughly calculating with a deviation of ±0.02 m/ns for the EM-wave velocity value that represents the frozen core, the calculated depth of a reflector at a two-way travel time of 25 ns below the frost table (e.g., R02: e) can vary by up to 0.5 m.

3.3 | Measurements of temperature and soil matric potential

Ground surface temperature (GST) data can provide valuable information on subsurface conditions, as the ground surface is the interface between the atmosphere and the subsurface and thereby controls the intensity of energy exchange processes. In this study, GST values were recorded hourly by M-Log data loggers (GeoPrecision GmbH), equipped with PT1000 sensors that provide an accuracy of ±0.1°C. Three sensors were distributed at different locations in the investigated area (see Figure 4 for locations and Table 5 for details): sensor T01 was placed outside the wetland in the surrounding desert, sensor T02 was placed on the surface of palsa OVR04, and sensor T03 was placed between two smaller, unnamed palsas. Values of daily mean temperature and MAGST values were calculated from the recorded data. For assumptions on the existence of an insulating snow cover, diurnal temperature variations were analyzed.[40,41] When diurnal temperature fluctuations were measured below 0.4 C throughout one complete day, the existence of an insulating snow cover is assumed.[42] So-called "zero-curtain" periods describe time spans in which surface temperatures are nearly constantly around 0°C. The appearance of nearly isothermal conditions is caused by latent heat that is bound in the phase change of water during freezing or thawing.[42,43]

The content of liquid water in the subsurface is an important variable that characterizes the ground thermal regime in frozen areas.[44,45] To approach this variable in our study, we measured the soil matric potential with Tensiomark sensors (ecoTech Umwelt-Messsysteme GmbH), an approach which is relatively new in periglacial geomorphology. The measurement principle is based on moisture-related variations in the heat capacity of a porous ceramic plate, which is measured with an artificial heat pulse. This requires a simultaneous recording of the temperature in the sediment surrounding the sensor.[46]

TABLE 4 Details of GPR profiles

Survey	Survey length (m)	Antenna frequency (MHz)	Time window (ns)	Temporal sampling interval (ps)	Number of stacks	Survey date
R01	72.5	100	200	800	4	Sep 6, 2017
R02	118	50	400	1,600	4	Sep 8, 2017
R03	20	200	100	400	4	Sep 6, 2017
R04	20	200	100	400	4	Sep 6, 2017
R05	45	200	100	400	4	Sep 6, 2017

TABLE 5 Detailed information on sensors

Position	Location	Measured parameter	Data collection rate (h^{-1})	Start of data acquisition	End of data acquisition
T01 surface	Surrounding desert	Temperature	1	Sep 20, 2015	Sep 19, 2017
T02 surface	Surface of palsa OVR04	Temperature	1	Sep 20, 2015	Sep 19, 2017
T03 surface	Wetland between palsas	Temperature	1	Sep 20, 2015	Sep 19, 2017
T02 (−0.5 m)	Surface of palsa OVR04	Temperature, pF-value	1	Sep 20, 2015	Dec 24, 2016
T03 (−0.55 m)	Wetland between palsas	Temperature, pF-value	1	Sep 20, 2015	Sep 19, 2017

Resulting dimensionless pF-values indicate the level of energy that is required to pull water out of the subsurface that is held by capillary and absorptive forces. A pF-value of 0 represents a state of full water saturation, while a value of 7 represents extremely dry conditions.[47] Compared to approaches that measure the volumetric water content,[48–50] the approach of measuring the soil matric potential has the advantage of not being bound to small sample volumes, which may be unrepresentative in heterogeneous settings. In contrast to measurements with tensiometers,[51] the Tensiomark device is frost-resistant. Soil matric potential data were acquired hourly at the same locations where the GST sensors T02 and T03 were placed (see Figure 4 for locations and Table 5 for details).

4 | RESULTS AND INTERPRETATION

4.1 | Central Palsa area

Horizontal slices of the ERI model E01 (Figure 5a) show a patchy resistivity distribution. Values of up to 1.9 kΩm appear in the center of the grid (A), at a position that corresponds to the center of palsa OVR01. This structure is interpreted as the frozen core of the palsa, which is covered by a 0.6-m-thick unfrozen layer that shows low resistivity values (around 0.4 kΩm). Maximum resistivity values in the center of the grid appear at the depth slice between 1.2 and 2 m. At greater depths, resistivity values decrease, but are still above 0.6 kΩm throughout the rest of the model (model thickness 5 m, last slice not shown).

Further resistivity values above the assumed threshold value of 0.6 kΩm appear in the northeastern (B) and the northwestern corner (C) of the grid. These positions correspond to rather unremarkable grassy areas next to palsa OVR01, where a few small mounds are visible at the ground surface. Comparable to the center of the grid, both structures extend through the entire depth of the model. While resistivity values in the northeastern corner (B) decrease constantly with increasing depth, resistivity values at the northwestern corner (C) increase from 0.7 kΩm directly below the surface to 1 kΩm at a depth of 2 m. Below 2 m, resistivity values at the northwestern corner (C) decrease slightly with increasing depth. Structures A and C appear to merge and represent one compound structure at this depth.

Markedly lower resistivity values (below 0.3 kΩm) dominate the horizontal resistivity distribution of the upper two slices of the E02 model (Figure 5b). In these slices, only a small gradual increase in resistivity towards the southeastern corner is visible. Below a depth of 1.2 m, the resistivity contrast between the southeastern corner, where cells reach up to 5 kΩm, and the rest of the model, where resistivity values are constantly below 0.3 kΩm, increases strongly. This forms a triangular structure of very high resistivity values (up to 11 kΩm at a depth of 3 m), which indicates frozen conditions (D). With further increasing depth, resistivity values change only slightly and at the bottom of the model, resistivity values are still above 9 kΩm (model thickness 5 m, last slice not shown). We interpret the outline of structure D and its position in the model to correspond to the location and perimeter of palsa OVR02.

In the partly overlapping ERI models E03 (Figure 6a), E04 (Figure 6b) and E05 (Figure 6c), resistivity values that indicate frozen conditions cluster in three larger (E, G, H) and one smaller structure (F). Note that the appearance of the smaller structure (F) is related to only a small number of data points in the measured apparent resistivity pseudosections. However, as the feature is visible in data from both surveys E03 and E04, we assume that its existence is realistic.

The positions of the four structures correspond to the occurrences of palsas at the ground surface but discrepancies exist between the horizontal extents of the high resistivity values and the
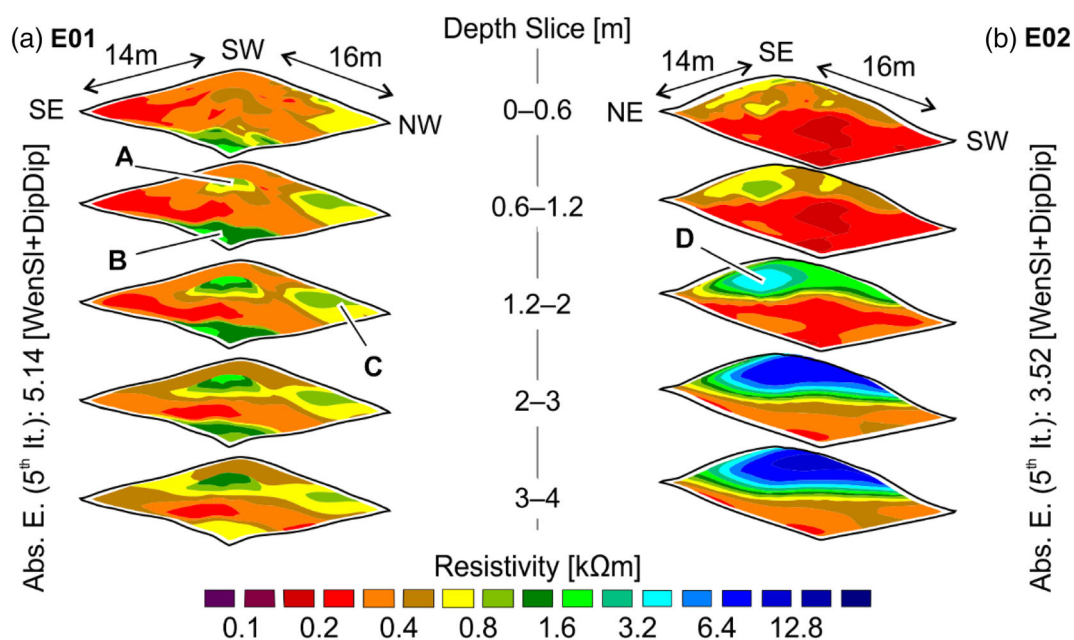

FIGURE 5 ERI models. (a) E01 and (b) E02. Selected model slices. Selected structures are labeled to raise visibility
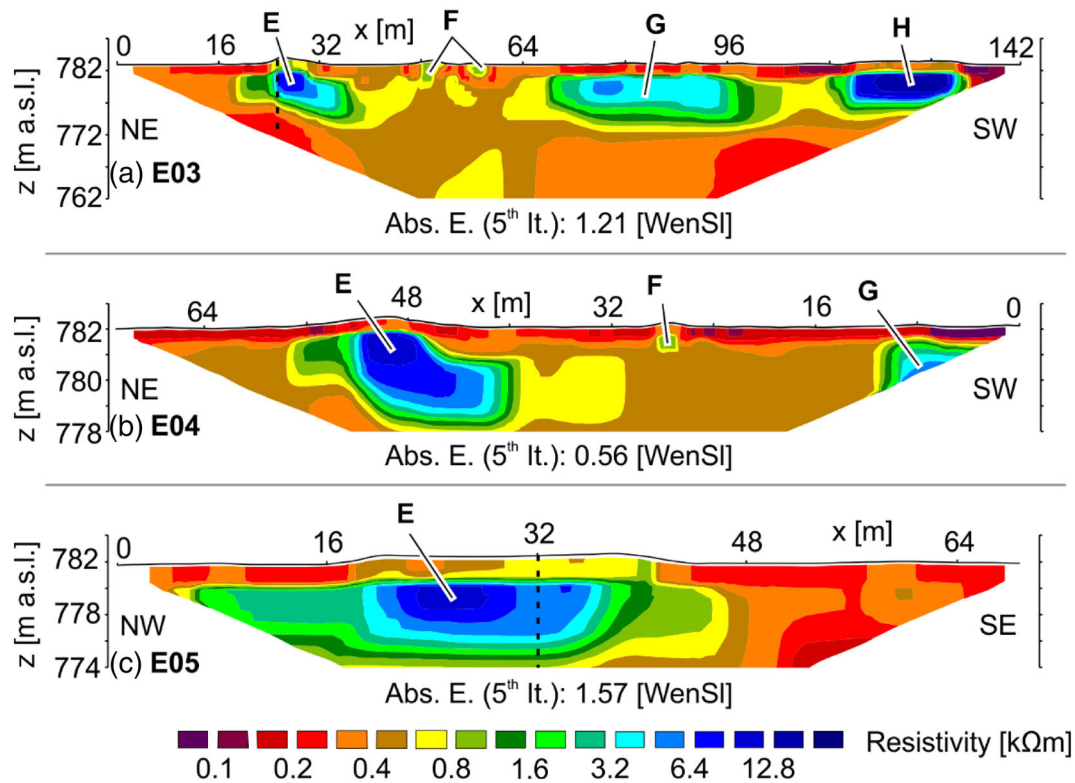
FIGURE 6 ERI models. (a) E03, (b) E04, and (c) E05. Dashed lines indicate intersections. Selected structures are labeled to raise visibility

uplifted areas. Resistivity structure E exceeds the uplifted area (which corresponds to palsa OVR02) in both horizontal directions. High-resistivity structures F and H are almost equal to the surface-uplifted areas (F: OVR01, H: unnamed palsa). The surface above the more extensive structure G is rather inconspicuous and barely uplifted at isolated positions.

While structures E, G and H show discrete lens-shaped outlines, structure F appears as two separated structures in the E03 model (Figure 6a). Except for structure F in the E03 model, all structures with resistivity values above the threshold are covered by an approximately 1- to 2-m-thick layer of low resistivity. Considering the threshold value of 0.6 kΩm, the E03 model shows extensively frozen subsurface conditions and a connection between structures E and F and between structures G and H. Lower resistivity values between structures E and F in the E04 model may be caused by slightly different surveying positions, a different spatial resolution of the two ERI models, or result from capturing a 2-D image of a complex 3-D feature. However, a disintegration of the connection between the two structures between the survey dates in 2015 and 2017 (see Table 3) cannot be ruled out.

Radargram R01 (Figure 7a) corresponds to a cross-section of the central palsa area. It is presented here as an overlay with the E04 model, which was measured at the same position. In the shallow subsurface, the radargram shows a layer with high signal attenuation, which we interpret to represent a layer with high water content. Below this layer, the radargram shows shallow continuous mostly surface conformable horizons (a) that change from a positive triplet sequence between 0 and 9 m along the x-axis of the radargram to a

negative triplet sequence at the position of the central palsas (between 9 and 44 m) and then trend back to a positive triplet sequence again (between 44 and 72 m). In the central part of the radargram, the depth of this pattern corresponds to the depth of the manually detected frost table, and the continuous horizon is hence interpreted to represent the frost table topography.

The positive triplet sequences at the margins of the radargram are interpreted to result from liquid water that accumulates at positions with a lowered frost table topography. The surface-parallel reflection pattern indicates eolian deposition of the subsurface materials, in agreement with the high rates of this deposition type in central Iceland.[35,52]

At a depth of around 1.9 m, the radargram shows a 1-m-thick patch with relatively low amplitude at a position of around 22 m along the x-axis (b). Its position corresponds to the appearance of structure E in the E04 model (see Figure 6b) and it is thus interpreted as a part of the frozen core of the palsa without internal stratigraphy. The appearance of further single reflectors with negative triplet sequences in deeper parts of the subsurface (e.g., c) are assumed to represent distinct ice layers within the frozen cores.

4.2 | Margin of the wetland and transition to central Palsa area

Higher resistivity values in the E06 model (Figure 8), compared to the ERI models of the central palsa area (E03–E05, Figure 6), indicate different subsurface conditions at the margin of the wetland. ERI model
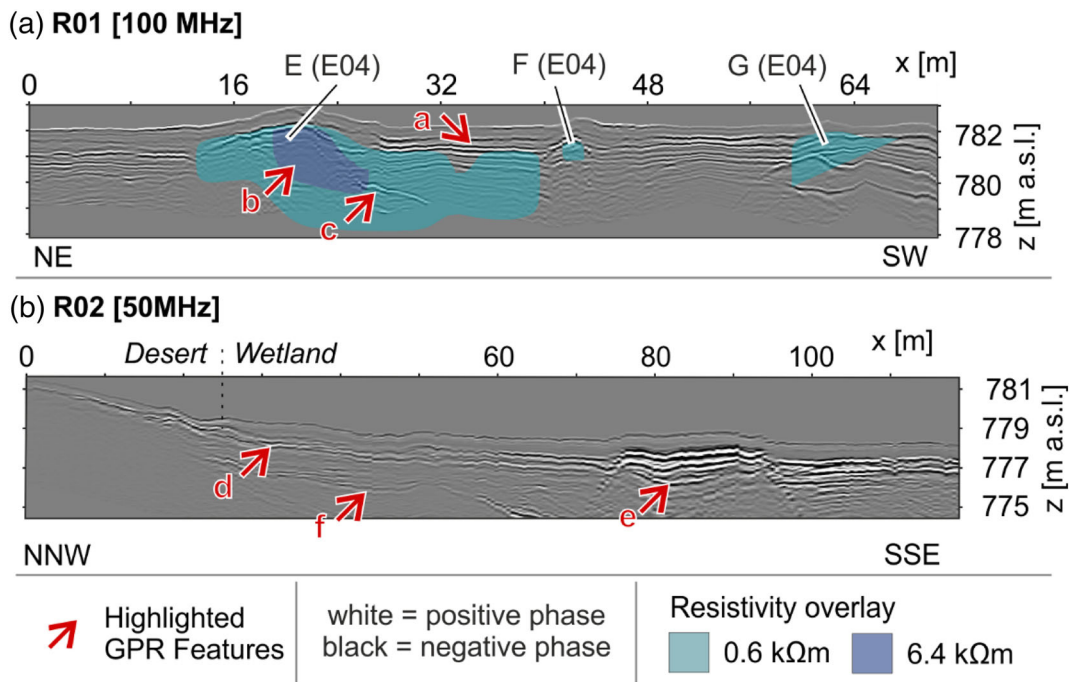
FIGURE 7 Radargrams overlaid with ERI data. (a) R01 with E04, (b) R02. Selected structures are labeled to raise visibility
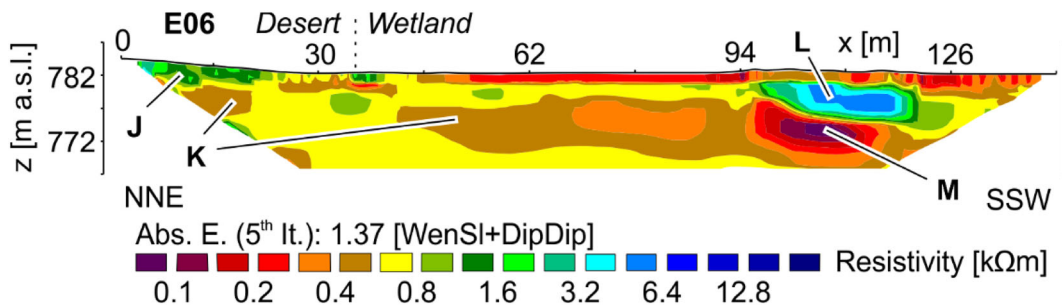

FIGURE 8 ERI model E06. Selected structures are labeled to raise visibility

E06 shows an upper layer of around 3 m thickness and high resistivity values of between 0.9 and 2.4 kΩm (J) in the part of the model that corresponds to the subsurface of the surrounding desert. Below this layer, resistivity values decrease to around 0.5 kΩm (K). In contrast to the upper layer, which appears only in the part of the model that corresponds to the surrounding desert, this lower layer can be traced through the complete length of the ERI model, except for an interruption of around 19 m at the transition between the two model parts (between 24 and 42 m along the x-axis). The part of the model that corresponds to the subsurface of the wetland shows a rather complex subsurface layering: maximum resistivity values are 5.8 kΩm and concentrate in a structure of up to 6 m thickness (L), which indicates the occurrence of ground ice. The horizontal extent of this structure corresponds to an area where two compound palsas form an uplifted area of around 0.6 m height. The structure is covered by a layer of 1.8 m thickness, which shows resistivity values below 0.5 kΩm. Below structure L, resistivity values decrease to a minimum of 0.1 kΩm (M).

From 0 to 75 m along the x-axis of Radargram R02 (Figure 7b), there is a continuous horizon that changes from a negative triplet sequence in the part that corresponds to the surrounding desert to a positive triplet sequence in the part that corresponds to the wetland (d). We interpret this as a continuous frost table, which is covered by coarse and dry materials with lower permittivity in the desert, while in the second part, it forms an impermeable boundary for surface water to infiltrate down and rest upon.

The horizon continues in the x-direction, and between 75 and 95 m along the x-axis, it raises towards the surface and the triplet sequence turns negative again. This indicates the occurrence of a deeper layer with a lower permittivity and, as this position corresponds to the location of an unnamed palsa, we interpret the horizon in this part of the radargram to represent the surface of the frozen core. At its margins (at around 75 m and at around 95 m along the x-axis) descending reflectors delimit an area with relatively high ice content.

From 95 to 120 m on the *x*-axis, the triplet sequence is again positive. This indicates that water, draining from the convex shape of the frozen core of the palsa, accumulates at this position, where the frost table acts as an impermeable boundary. Multiple convex reflectors down to a depth of around 2 m (e.g., e) indicate multiple layers of ice within the frozen core. Between 25 and 75 m along the *x*-axis of the radargram, there is an undulating reflector with a positive triplet sequence at a depth of around 3 m (f). Considering the E06 model, which shows decreasing resistivity values at a comparable position (E06: K), this reflector is interpreted to represent a transition towards a zone with a higher content of liquid water.

4.3 | Northern Palsa area

ERI model E07 (Figure 9a) shows a rather homogeneous distribution of resistivity in the subsurface of palsa OVR03, compared to the other ERI models. The upper two depth slices comprise resistivity values between 0.8 and 2.1 kΩm. This indicates frozen conditions and shows that the model fails to resolve any thaw zone. In the following depth slice, resistivity values increase sharply to around 8 kΩm in the center of the model (N). With increasing depth, resistivity values reach up to 48 kΩm (depth slice 2–3 m) and 89 kΩm (depth slice 3–4 m). Between a depth of 4 m and the bottom of the model (model thickness 5 m, last slice not shown), resistivity values reach up to 100 kΩm.

Two structures (P, Q) of high resistivity appear in the ERI model E08 (Figure 9b), which represents a cross-section of the palsas OVR03 and OVR04 and the gap in between. Both structures are located at positions that correspond to the subsurface of the two palsas and reach resistivity values of up to 98 kΩm (P) and 89 kΩm (Q). They are separated by a zone of extremely low resistivity values, between 0.01 and 0.4 kΩm (R). This zone stretches over a length of 12 m and its position corresponds to the transition between the two palsas. However, only a small part of the structure corresponds to the water-covered part of the gap. Resistivity values above the two structures of high resistivity are greater than 1 kΩm and increase sharply below depths between 1 and 2 m. A lower boundary of the structures can be detected at depths between 10 m (P) and 6 m (Q).

The intersecting ERI models E09 (Figure 10a) and E10 (Figure 10b) represent cross-sections along the longitudinal (E09) and the transverse (E10) axis of palsa OVR05. Model E09 shows a lens-shaped structure of around 1 m thickness and resistivity values of between 0.6 and 3 kΩm (S), which is interpreted as the frozen core of the palsa. Model E10 shows a higher thickness of this structure and markedly higher resistivity values, up to nearly 9 kΩm. Only the transverse E10 model but not the longitudinal E09 model shows the appearance of an additional structure of high resistivity (T) that is separated from the main structure and shows resistivity values of up to 0.8 kΩm. The position of the gap between the two structures matches with the location of a crack on the palsa surface (see Figure 2d). However, the appearance of the smaller structure is related to a decrease of only a few data points in the measured apparent resistivity pseudo-section and must hence be interpreted carefully.

Radargram R03 (Figure 11a) corresponds to a longitudinal cross-section of palsa OVR05. It is dominated by a surface-parallel reflection horizon, which is interpreted to represent eolian deposits.[35] Directly below the surface in the center of the radargram (between 9 and 14 m along the *x*-axis), prominent reflectors with positive
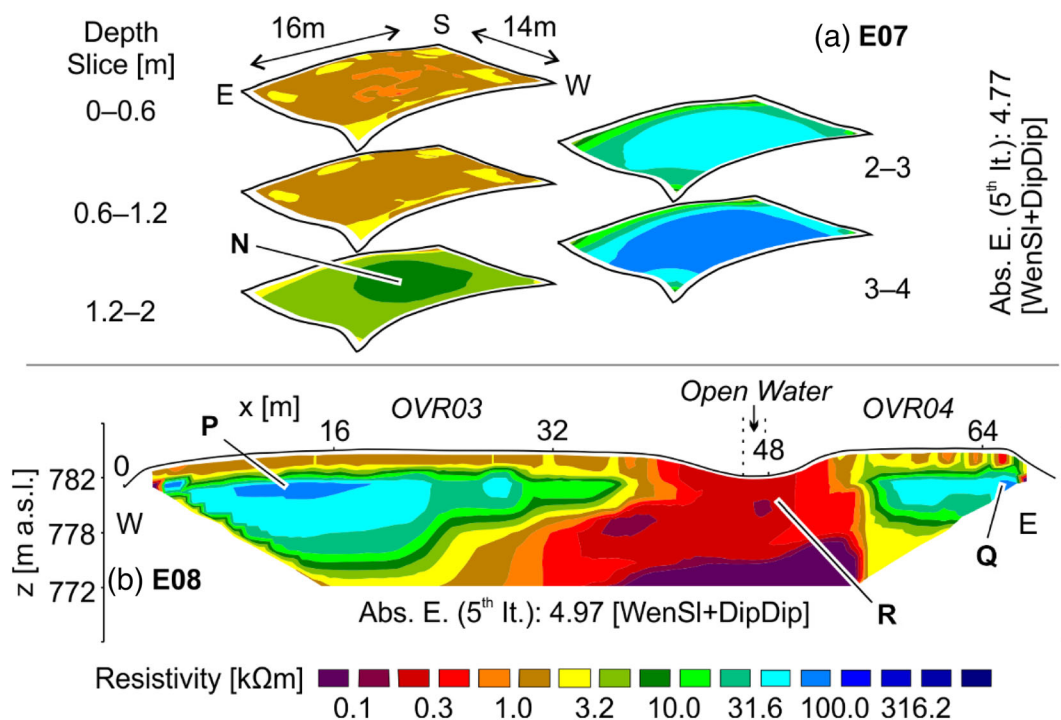

FIGURE 9 ERI models. (a) E07 and (b) E08. Selected model slices. Selected structures are labeled to raise visibility
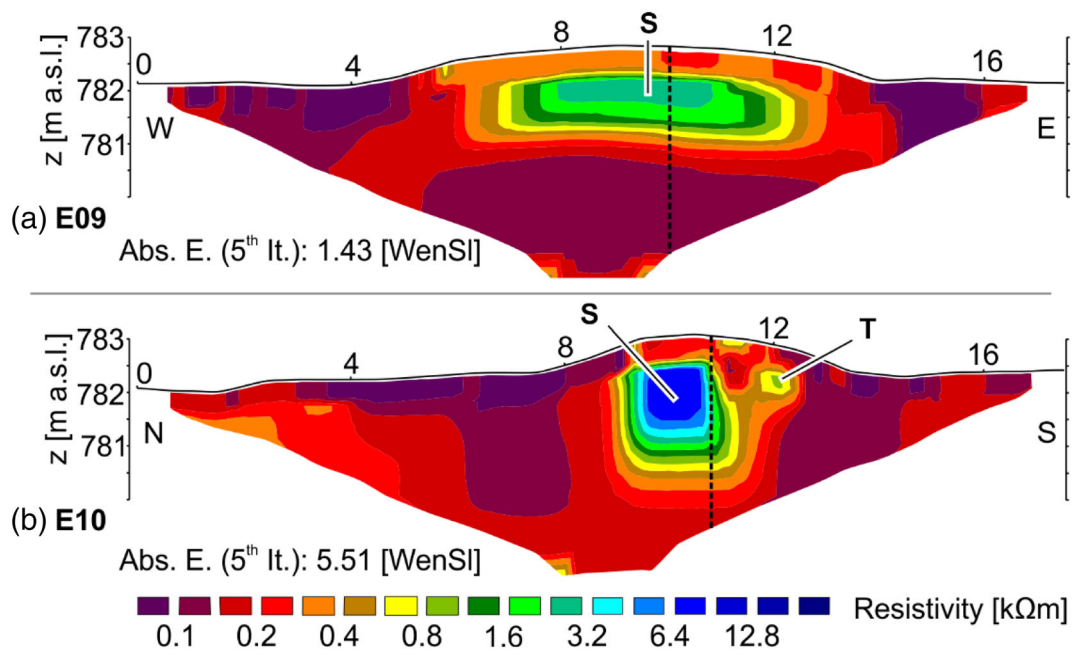
FIGURE 10 ERI models. (a) E09 and (b) E010. Selected model slices. Dashed lines indicate intersections. Selected structures are labeled to raise visibility
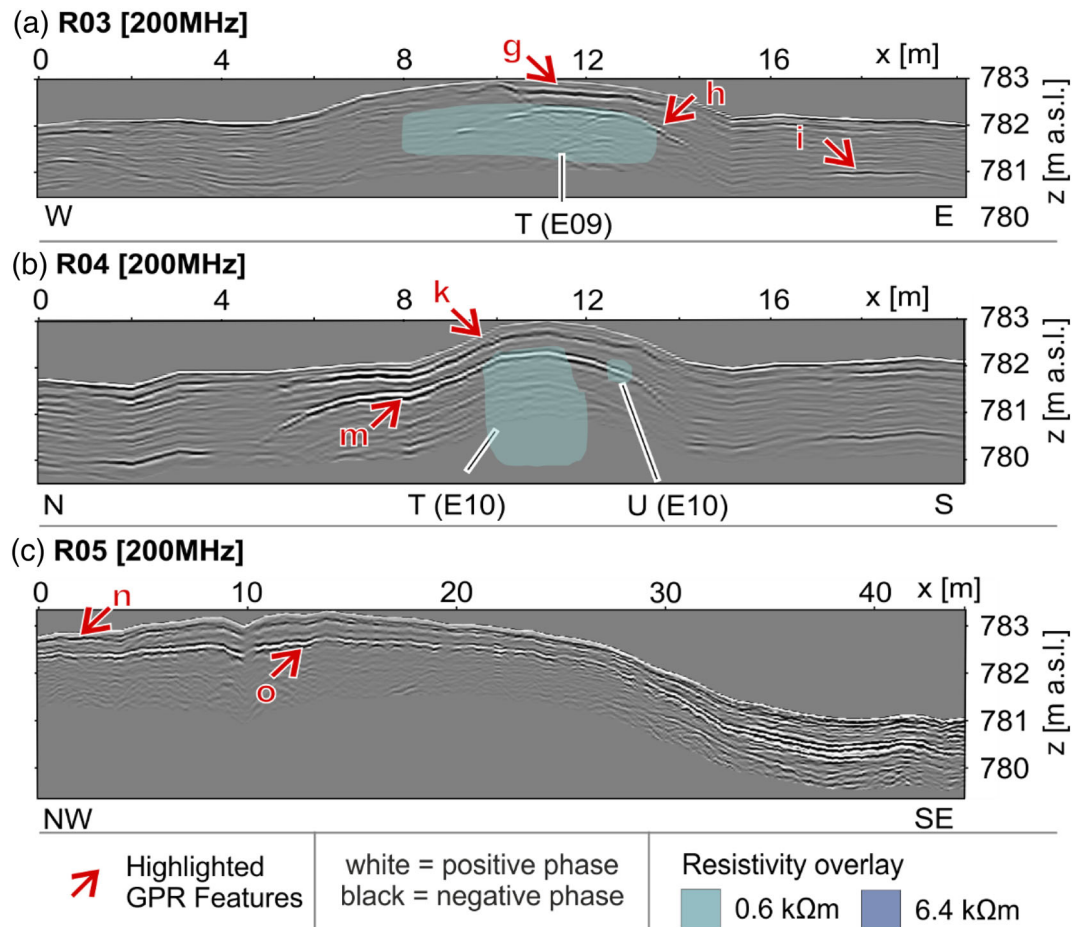

FIGURE 11 Radargrams overlaid with ERI data. (a) R03 with E09, (b) R04 with E10, and (c) R05. Selected structures are labeled to raise visibility

triplet sequences appear (g). They are interpreted to represent alternating layers of different types of subsurface materials and their differences in water content. This agrees with the different layers of sandy loam and loam in the area, which were reported in a previous study.[23]

At a depth of around 0.5 m is a prominent reflector with a negative triplet sequence (h). Its depth matches a resistivity increase in the corresponding E09 model and as the negative triplet sequence indicates a transition towards higher permittivity in the deeper layer, this reflector is assumed to represent the boundary of the frozen core. Reflectors with positive triplet sequences in the deeper parts of the subsurface next to the palsa (e.g., i) are interpreted as accumulations of liquid water on an impermeable boundary.

The perpendicular R04 radargram shows a similar surface-parallel reflection pattern (Figure 11b). Between 5 and 14 m along the x-axis of the radargram, there is a horizon with a positive triplet sequence at a depth between 0.2 and 0.3 m (k). It is interpreted as a transition between layers of different subsurface materials. The higher amplitude of this horizon at the margin of the palsa (between 6 and 9 m along the x-axis) indicates accumulations of liquid water at this position. At 12 m along the x-axis of the radargram, where the survey line intersects with the surface crack (see Figure 2d), this horizon appears to descend slightly. However, this observation may also be caused by difficulties in data acquisition in the rough environment. Below this horizon, one prominent reflector with a negative triplet sequence is visible (m) and, as its depth of around 0.5 m aligns with the resistivity increase in the E10 model, is interpreted as the upper edge of the frozen core. In contrast to the E10 model, where results indicate a local deepening of the frost table, there is no indication of this in radargram R04. At the margins of the radargram, between 0 and 4 m along the x-axis and between 14 and 20 m along the x-axis, reflectors with positive triplet sequences at a depth of around 2 m indicate accumulations of liquid water on an impermeable boundary.

Between 0 and 25 m along the x-axis of radargram R05, which corresponds to a cross-section of palsa OVR04 (Figure 11c), the radargram shows a reflector with a positive triplet sequence directly below the surface (n). We interpret this to represent structural differences, as the occurrence of the frost table at this shallow depth can be ruled out. Around 0.5 m below this upper reflector, a lower reflector, traceable throughout the entire radargram, appears (o). Between 0 and 30 m along the x-axis, it has a negative triplet sequence. This indicates a transition towards a lower permittivity and, hence, the reflector is interpreted to represent the frost table. The triplet sequence turns positive and the reflector changes to a thicker horizon after around 30 m along the x-axis of the radargram, which corresponds to the edge of the palsa. We assume that the frost table acts as an impermeable boundary at this position, on which water draining from the frozen core of the palsa accumulates. This local increase in liquid water within the active layer enhances the dielectric contrast between the frozen and the unfrozen layer and causes the higher reflection amplitudes in this part of the radargram.

4.4 | Temperature and water potential measurements

At the sensor position in the surrounding desert (T01), daily mean temperature values between 19.5 and $-16.5°$C were recorded between September 20, 2015 and September 20, 2017 (Table 6). Values fluctuated strongly throughout the complete investigated time span and the curve of recorded GST values lacks durable periods of zero-curtain conditions (Figure 12a). A similar temperature curve, but with slightly damped values and a short period of zero-curtain conditions, is derived from the GST records at T02 (Figure 12b). At this sensor position, located at the surface of OVR04, higher minimum values ($-14.3°$C) and lower maximum values (14.0°C) were recorded. Records of both GST sensors indicate mostly snow-free conditions, probably due to snow redistribution by wind. This explains the strong variations of MAGST values between the different sensor positions and the inconsistent development of zero-curtain periods (see Table 6).

The GST plot of sensor T03 (Figure 12c), located between two palsas, resembles the curves of T01 and T02 only during summer. Based on the absence of extremely low temperature values (lowest value was $-2.74°$C), it indicates that a durable snow cover developed at this position. The maximum daily mean temperature value of 12.5°C was recorded at the same date as the maxima of the other sensors, in July 2017. In both years, the GST plot of T03 shows a relatively long period of zero-curtain conditions compared to the other sensors. The total number of days with zero-curtain conditions decreased at the sensor locations T02 and T03 between 2015 and 2016, while the number slightly increased at T01. Interannual differences in MAGST values between the sensor locations, however, are in a similar range (see Table 6).

TABLE 6 Results of temperature measurements. MAGST = mean annual ground surface temperature, T = temperature, SC=snow cover

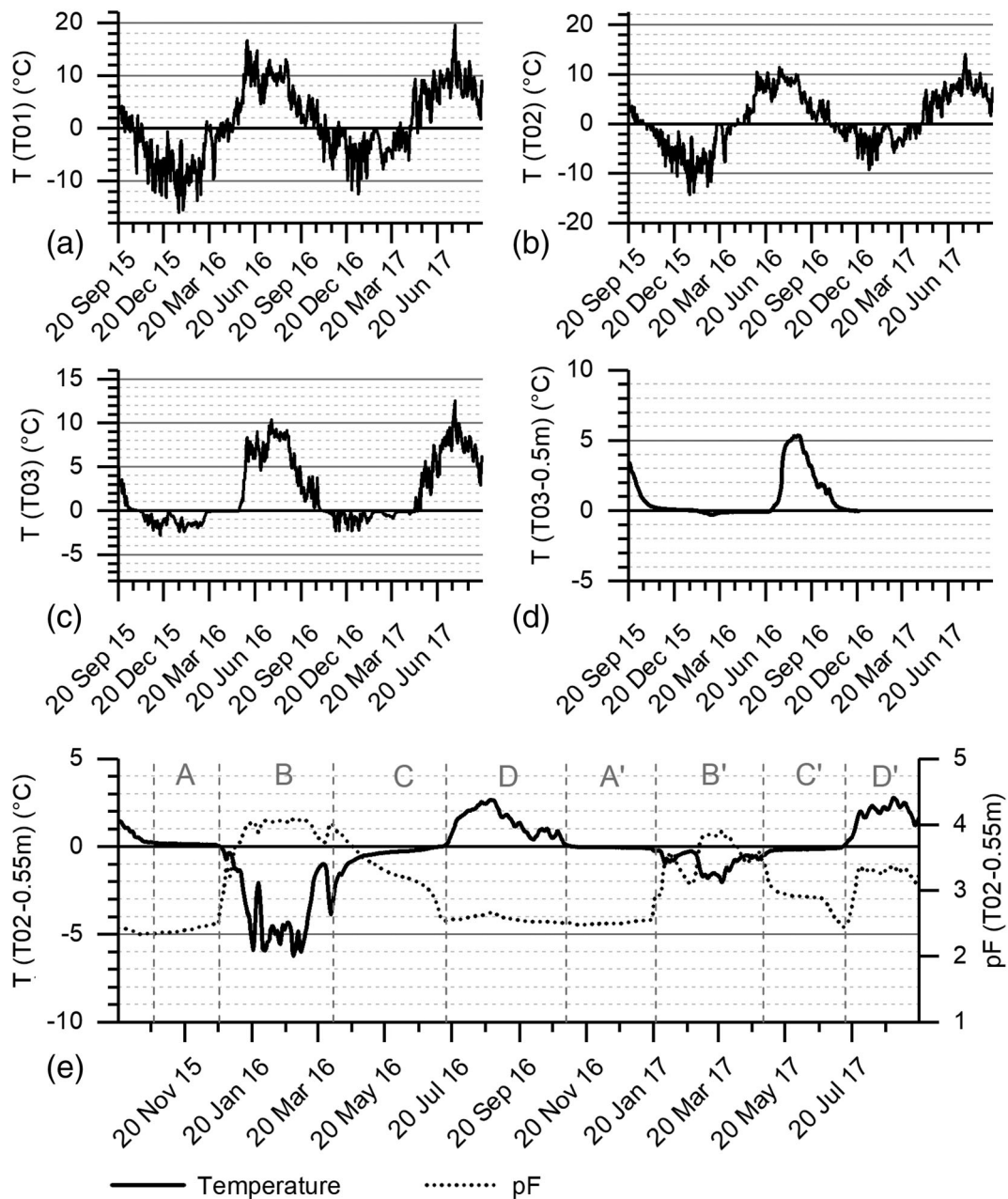|	MAGST (°C) (2015/09/20–2016/09/20)	MAGST (°C) (2016/09/20–2017/09/20)	T (max/min) (°C)	SC (days) (2015/09/20–2016/09/20)	SC (days) (2016/09/20–2017/09/20)
T01 surface	0.30	1.56	19.5/−16.5	0	10
T02 surface	0.25	1.52	14.0/−14.3	54	41
T03 surface	1.09	2.21	12.5/−2.7	186	160
T02 (−0.5 m)	−0.67	0.16	2.8/−6.2	—	—
T03 (−0.55 m)	0.94	No data	5.4/−0.3	—	—

FIGURE 12 Temperature curves and pF-value plots

The combined plot of the recorded subsurface temperature values and matric potential values at T02 (Figure 12e) can be divided into four phases, which highlight the ability of liquid water to buffer temperature variations in the active layer: Between mid-October 2015 and mid-December 2015, subsurface conditions were quite stable: temperature values varied slightly around 0°C and pF-values varied slightly around 2.4 (Phase A). This phase ended in mid-December 2015 with an increase of pF-values and a nearly simultaneous decrease in temperature. It was followed by a phase of high pF-values and subzero temperatures (Phase B), in which short-term temperature fluctuations coincided with similar fluctuations of pF-values. Phase B lasted until early April 2016 and was followed by a transitional phase (Phase C). Phase C was characterized by gradually

increasing temperatures that approached 0°C, and by gradually decreasing pF-values. This observation highlights that subsurface materials can hold a relatively large amount of liquid water, although they are frozen. The subsequent phase (Phase D) started in early July 2016, when daily mean temperatures started to be constantly positive and pF-values reached a minimum level on which they remained for the next 6 months. After Phase D, which started in early November 2016, this cycle was repeated (A'–D').

Differences between the two cycles mainly concern the magnitude of the recorded temperature and matric potential values and are attributed to intra-annual variations. However, one distinct difference between the two years of investigation concerns the beginning of the phases D and D': in the second cycle, pF-values increased

exceptionally strongly after mid-July 2017. It is conceivable that a period of extraordinary high evaporation led to desiccation in this part of the active layer, as all GST sensors show their maximum temperature values around this time of the year.

Positive subsurface temperature values (Figure 12d) and the absence of any pF-value variations at T03 (data not shown) through the complete investigated time span indicate that the subsurface at this position was permanently in an unfrozen, water-saturated state and that the maximum frost depth is thus lower than 0.5 m. However, it must be noted that the lack of any fluctuations from the displayed pF-value of 0 is suspicious and may indicate malfunction, especially as the sensor failed completely in December 2016.

5 | DISCUSSION

5.1 | Methodological aspects

Only 12 out of the 9,366 data points that were measured in total were obviously erroneous and had therefore been removed during processing of the geoelectrical data sets. This emphasizes the exceptionally high data quality, regarding ground coupling and other external sources of disturbances in data acquisition. The relatively low absolute error values of the presented ERI models show that suitable inversion settings were chosen.

Although the more robust Wenner–Schlumberger array is commonly recommended for investigations in permafrost environments due to its higher signal strength,[53] surveying with a dipole–dipole electrode configuration also provided plausible results. When surveys using dipole–dipole and Wenner–Schlumberger arrays were performed comparatively, inversion models showed comparable resistivity distributions (see Figure 3a,b). Problems in detecting the lower limit of permafrost bodies, as reported from other studies,[21] were avoided by using an L1-norm inversion scheme.[54] Unfortunately, the thicknesses of the thaw zone could not be resolved in ERI models E07 and E08.

Discrepancies between the adjacent and partly overlapping models E03, E04 and E05 are attributed to geometrical variations between the positions of the survey lines, differences in the electrode spacing, and temporal alterations between the survey dates (see Table 3). However, it is also conceivable that these differences indicate "3-D effects."[55,56] These effects, which result from complex resistivity distributions, are considered to represent a main drawback of the 2-D ERI approach.[56] They are probably responsible for the differences between the intersecting 2-D ERI models E09 and E10, as well.

The threshold value of 0.6 kΩm to distinguish between frozen and unfrozen subsurface conditions is relatively low, but plausible regarding observations from other palsa and lithalsa sites, where values are only slightly higher.[14,15,20,21] It reflects the fine-grained materials, which can store a relatively high amount of liquid water when temperatures are at 0°C or even slightly below.[16,21,57,58]

Crucial for a successful application of GPR is a sufficiently good coupling between the antennas and the ground surface.[59–61] In our study, problems with weak coupling may have occurred only at positions where the antennas could not be placed planar on the ground, such as due to an undulating surface topography or at positions with a low scrub vegetation. In such cases, we changed the antenna orientation from perpendicular broadside to oblique to increase signal response.[62] Subsequent disturbance of the electromagnetic field can be neglected, as the occurrence of linear objects in the subsurface is not assumed at the study area.[63] Only in the R03 radargram is a slight effect of weak ground coupling assumed, as the observed weakening in reflection amplitude coincides with positions where the antennas were moved along the surface crack of OVR05. However, it is also conceivable that the surface crack altered the physical properties of the subsurface materials, which caused the lower reflection amplitude.

Compared to other investigations in permafrost environments using center frequencies between 25 and 200 MHz,[20,64–66] the observed penetration depths are relatively low. This can probably be attributed to a relatively high amount of liquid water in the subsurface and the accompanying signal attenuation.[67] The influence of highly attenuative sediments cannot be assessed, as no information on ground truth (e.g., pits, cores) is available.

5.2 | Palsa development

The different stages of cyclic palsa development are described and depicted in block figures by Seppälä.[1,68] The following interpretations are based on these stages.

Despite relatively high MAGST values, the recorded GST curves agree with the assumption of permafrost-favorable conditions at the Orravatnsrústir Palsa Site, as indicated by previous studies.[7,8,23] GST records from the surrounding desert (T01) indicate snow-free conditions outside the wetland area, but, despite the relatively low temperatures and the assumed existence of a continuous frost table, larger occurrences of ground ice are unlikely in this part of the study area. This is due to the relatively low frost susceptibility of the comparatively coarse-grained materials outside the wetland[69] and is expressed by the absence of high resistivity values in the corresponding part of the E06 model. However, we note that our interpretation of a continuous frost table in the surrounding desert (R02: d) is not backed by ground truth data (e.g., cores, frost-probing).

The appearance of a nearly continuous layer of relatively low resistivity values in the E06 ERI model (E06: K) indicates that the coarse-grained materials (E06: J) only form a cover layer. Mainly snow-free conditions at OVR04 (T02) facilitate the penetration of low winter temperatures and thus contribute to the shallow thickness of the thaw zone of this palsa, which is resolved only in radargram R05 (R05: o) and ranges between 0.7 and 0.9 m. The appearance of resistivity values up to nearly 100 kΩm at OVR03 and 90 kΩm at OVR04 indicates massive aggregations of ice, but it must be noted that the magnitude of resistivity may be enhanced by the palsa height and a

subsequent gravitational loss of liquid water from the uplifted layers. The resistivity gradient may be further enhanced by the open water in the surrounding of the palsas.

The correlation between MAGST values and snow cover duration at the GST sensor positions (see Table 6) emphasizes the close coupling of these two parameters and the importance of snow-free periods for palsa formation and development.[1] The observed ability of the subsurface materials to hold a relatively high amount of liquid water even in a frozen state, as shown by the recorded pF-values and subsurface temperatures, agrees with findings from other studies in peaty materials[43] and is presumably transferable to other study sites. However, subsurface materials at Orravatnsrústir differ from the subsurface materials in other palsa areas by a relatively low organic content and a high content of sand.[23]

The ratio between palsa height and permafrost thickness at palsa OVR01 is around 1:3, which is characteristic for a palsa that is freely uplifted by buoyancy forces.[6,22] Hence, it is unlikely that the visually observed signs of degradation at this palsa, that is the sunken appearance and the water pond (see Figure 2a), can be attributed to a mature stage of palsa development, which starts only after the frozen core has reached the bottom of the water-saturated layer.[68] More probably, these signs of degradation indicate bottom-up melting[1]: this concept describes the beginning of shrinking of a frozen palsa core due to environmental changes, such as changes in water level, climatic changes or small-scale variations in snow cover, before it has reached the bottom of the water-saturated layer.[70] Shrinking continues until only a small dome-shaped structure is left, which rises out of the water.

At palsa OVR02, the discrepancy between the relatively small extent of the frozen core and the relatively large extent of the uplifted area can be explained only if the uplift by buoyancy forces is restrained, for example by the absence of liquid water below the ice layers.[22] This phenomenon is usually connected to a mature state of palsa development and occurs when the growing core has reached the bottom of the water-saturated layer.[1] However, a mature state of palsa development contradicts the assumption that OVR02 belongs to the newly formed palsas that developed after the 1960s.[7,8,23] Both observations can be combined if the occurrence of a compound structure of ice is assumed. This is indicated by the horizontal reflector within the frozen core in the corresponding radargram (R01: c). When only the thickness of the upper part of the core of OVR02 is used for calculating the ratio between palsa height and permafrost thickness, a value is received that aligns with an initial development stage.[21]

A compound palsa core may have formed when the growing ice layers of palsa OVR02 reached a pre-existing frozen structure at the bottom of the water-saturated layer. Such structures at the bottom of the water-saturated layer, however, are only rarely described in the literature. They may originate from remnant ice of decomposed palsas,[71] but it must be noted that this is speculative.

The results indicate a deceleration of active layer thickening at palsas OVR03 and OVR04, as the detected values are similar to those from 2010.[23] However, active layer thickness is generally low, considering the large size of the palsas.[1] This is attributed to surface abrasion, caused by strong winds on the exposed palsa surfaces.[72] The

distinct surface crack at palsa OVR05 is not necessarily a sign of decay, as the formation of cracks on the surface of palsas is not only bound to permafrost degradation: dilation due to palsa uplift can also cause surface cracking, especially in an early stage of palsa development.[10] This is probably the case at OVR05, as the ratio between palsa height and permafrost thickness indicates such an initial development stage.[6,21]

6 | CONCLUSIONS

The present findings highlight the ability of the internal structure to archive past environmental conditions and landforming processes. Thus, it provides valuable information for an enhanced understanding of the development of palsas and other periglacial landforms. The applied methods are suitable to differentiate between palsas of different development stages, although they occur in close proximity, and may be transferred to other study areas. Our study affirms the assumed long history of palsa development at the Orravatnsrústir Palsa Site but shows that the area has recently faced environmental changes. However, it must be emphasized that the assumed existence of frozen cores from decomposed palsas is precarious and only rarely described in other studies. Therefore, this needs to be clarified by further investigations. The investigated palsas are assigned to the following stages:

- Palsa OVR01 represents an initial development stage. However, its growth stopped and the palsa is now affected by bottom-up melting. This is an indication for recently changing environmental conditions.
- Palsa OVR02 also represents an initial development stage, but geophysical results indicate that palsa growth stopped when the growing core reached a pre-existing frozen structure at the bottom of the water-saturated layer.
- Palsas OVR03 and OVR04 represent stages of palsa decay. Both palsas show strong signs of lateral degradation but still comprise massive ice layers.
- Despite its surface crack, palsa OVR05 presumably represents an initial development stage.

The recording of pF-values can add valuable ground truth information on the state of the subsurface. Although this information did not decisively change the conclusions of this study, the installation of a higher number of sensors and their positioning at different vertical levels of the permafrost profile can be helpful for future research, for example to investigate melting processes of the frozen core.

DATA AVAILABILITY STATEMENT

Geophysical data are available upon request from the authors.

ORCID

Adrian Emmert https://orcid.org/0000-0003-2277-0041
Christof Kneisel https://orcid.org/0000-0002-5348-9001

REFERENCES

1. Seppälä M. Synthesis of studies of palsa formation underlining the importance of local environmental and physical characteristics. *Quatern Res*. 2011;75(2):366-370.
2. Jones PD, Moberg A. Hemispheric and large-scale surface air temperature variations: An extensive revision and an update to 2001. *J Climate*. 2003;16(2):206-223.
3. Borge AF, Westermann S, Solheim I, Etzelmüller B. Strong degradation of palsas and peat plateaus in northern Norway during the last 60 years. *Cryosphere*. 2017;11(1):1-16.
4. Zuidhoff FS, Kolstrup E. Changes in palsa distribution in relation to climate change in Laivadalen, northern Sweden, especially 1960–1997. *Permafr Periglac Process*. 2000;11(1):55-69.
5. Sjöberg Y, Coon E, Sannel ABK, et al. Thermal effects of groundwater flow through subarctic fens: A case study based on field observations and numerical modeling. *Water Resour Res*. 2016;52(3):1591-1606.
6. Allard M, Rousseau L. The international structure of a pala and a peat plateau in the Rivière Boniface region, Québec: Interferences on the formation of ice segregation mounds. *Géogr Phys Quatern*. 1999;53(3):373-387.
7. Kneisel C. The nature and dynamics of frozen ground in alpine and subarctic periglacial environments. *Holocene*. 2010;20(3):423-445.
8. Hirakawa K. Development of palsa bog in central highland, Iceland. *Geogr Rep Tokyo Metropolitan Univ*. 1986;21:111-122.
9. Kuhry P. Palsa and peat plateau development in the Hudson Bay Lowlands, Canada: timing, pathways and causes. *Boreas*. 2008;37(2):316-327.
10. Matthews JA, Dahl SO, Berrisford MS, Nesje A. Cyclic development and thermokarstic degradation of palsas in the mid-alpine zone at Leirpullan, Dovrefjell, Southern Norway. *Permafr Periglac Process*. 1997;8(1):107-122.
11. Oksanen PO. Holocene development of the Vaisjeäggi palsa mire, Finnish Lapland. *Boreas*. 2006;35(1):81-95.
12. Zuidhoff FS, Kolstrup E. Palsa development and associated vegetation in northern Sweden. *Arct Antarct Alp Res*. 2005;37(1):49-60.
13. Iwahana G, Fukui K, Mikhailov N, Ostanin O, Fujii Y. Internal structure of a lithalsa in the Akkol Valley, Russian Altai Mountains. *Permafr Periglac Process*. 2012;23(2):107-118.
14. Dobiński W. Geophysical characteristics of permafrost in the Abisko area, northern Sweden. *Pol Polar Res*. 2010;31(2):141-158.
15. Fortier R, LeBlanc AM, Allard M, Buteau S, Calmels F. Internal structure and conditions of permafrost mounds at Umiujaq in Nunavik, Canada, inferred from field investigation and electrical resistivity tomography. *Can J Earth Sci*. 2008;45(3):367-387.
16. Kneisel C, Saemundsson T, Beylich A. Reconnaissance surveys of contemporary permafrost environments in central Iceland using geoelectrical methods: implications for permafrost degradation and sediment fluxes. *Geogr Ann: Ser A, Phys Geogr*. 2007;89(1):41-50.
17. Wolfe SA, Stevens CW, Gaanderse AJ, Oldenborger GA. Lithalsa distribution, morphology and landscape associations in the Great Slave Lowland, Northwest Territories, Canada. *Geomorphology*. 2014;204:302-313.
18. Doolittle J, Hardisky M, Black S. A ground-penetrating radar study of Goodream palsas, Newfoundland, Canada. *Arct Antarct Alp Res*. 1992;24(2):173-178.
19. Kohout T, Bućko MS, Rasmus K, Leppäranta M, Matero I. Non-invasive geophysical investigation and thermodynamic analysis of a palsa in Lapland, Northwest Finland. *Permafr Periglac Process*. 2014;25(1):45-52.
20. Sjöberg Y, Marklund P, Pettersson R, Lyon SW. Geophysical mapping of palsa peatland permafrost. *Cryosphere*. 2015;9(2):465-478.
21. Lewkowicz AG, Etzelmüller B, Smith SL. Characteristics of discontinuous permafrost based on ground temperature measurements and electrical resistivity tomography, southern Yukon, Canada. *Permafr Periglac Process*. 2011;22(4):320-342.
22. Seppälä M, Kujala K. The role of buoyancy in palsa formation. *Geol Soc Lond Spec Publ*. 2009;320(1):51-56.
23. Saemundsson T, Arnalds O, Kneisel C, Jonsson HP, Decaulne A. The Orravatnsrustir palsa site in Central Iceland—Palsas in an aeolian sedimentation environment. *Geomorphology*. 2012;167:13-20.
24. Pissart A. Palsas, lithalsas and remnants of these periglacial mounds. A Progress Report. *Permafr Periglac Process*. 2002;26(4):605-621.
25. Jóhannesson H. Geologic Map of Iceland. 1:600 000. Bedrock Geology 2014. Icelandic Institute of Natural History. https://gatt.lmi.is/geonetwork/srv/eng/catalog.search#/metadata/%7B005FFDAD-69A1-4385-B16F-FD31B960FE33%7D
26. Hauck C. New concepts in geophysical surveying and data interpretation for permafrost terrain. *Permafr Periglac Process*. 2013;24(2):131-137.
27. Reynolds JM. *An introduction to applied and environmental geophysics*. Hoboken, NJ: John Wiley & Sons; 2011.
28. Kneisel C, Hauck C, Fortier R, Moorman B. Advances in geophysical methods for permafrost investigations. *Permafr Periglac Process*. 2008;19(2):157-178.
29. Emmert A, Kneisel C. Internal structure of two alpine rock glaciers investigated by quasi-3-D electrical resistivity imaging. *Cryosphere*. 2017;11(2):841-855.
30. Loke MH. *Tutorial: 2-D and 3-D electrical imaging surveys*. Malaysia: Geotomosoft; 2016 https://www.geotomosoft.com/coursenotes.zip. Accessed March 29, 2020.
31. Stummer P, Maurer H, Horstmeyer H, Green AG. Optimization of DC resistivity data acquisition: Real-time experimental design and a new multielectrode system. *IEEE Trans Geosci Remote Sens*. 2002;40(12):2727-2735.
32. Wilkinson PB, Meldrum PI, Chambers JE, Kuras O, Ogilvy RD. Improved strategies for the automatic selection of optimized sets of electrical resistivity tomography measurement configurations. *Geophys J Int*. 2006;167(3):1119-1126.
33. Moorman BJ, Robinson SD, Burgess MM. Imaging periglacial conditions with ground-penetrating radar. *Permafr Periglac Process*. 2003;14(3):319-329.
34. Scott W, Sellmann P, Hunter J. Geophysics in the study of permafrost. *Geotech Environ Geophys*. 1990;1:355-384.
35. Van Overmeeren R. Radar facies of unconsolidated sediments in The Netherlands: A radar stratigraphy interpretation method for hydrogeology. *J Appl Geophys*. 1998;40(1–3):1-18.
36. Arcone SA, Lawson DE, Delaney AJ. Short-pulse radar wavelet recovery and resolution of dielectric contrasts within englacial and basal ice of Matanuska Glacier, Alaska, USA. *J Glaciol*. 1995;41(137):68-86.
37. Delisle G, Allard M, Fortier R, Calmels F, Umiujaq LÉ. Northern Québec: innovative techniques to monitor the decay of a lithalsa in response to climate change. *Permafr Periglac Process*. 2003;14(4):375-385.

38. Hinkel K, Doolittle J, Bockheim J, et al. Detection of subsurface permafrost features with ground-penetrating radar, Barrow, Alaska. *Permafr Periglac Process*. 2001;12(2):179-190.

39. Horvath CL. An evaluation of ground penetrating radar for investigation of palsa evolution, MacMillan Pass, NWT, Canada. Proceedings of the Seventh International Conference on Permafrost, Yellowknife, Canada 1998;57:473-478.

40. Lewkowicz AG. Evaluation of miniature temperature-loggers to monitor snowpack evolution at mountain permafrost sites, Northwestern Canada. *Permafr Periglac Process*. 2008;19(3):323-331.

41. Reusser DE, Zehe E. Low-cost monitoring of snow height and thermal properties with inexpensive temperature sensors. *Hydrol Process*. 2011;25(12):1841-1852.

42. Rödder T, Kneisel C. Influence of snow cover and grain size on the ground thermal regime in the discontinuous permafrost zone, Swiss Alps. *Geomorphology*. 2012;175:176-189.

43. French HM. *The Periglacial Environment*. *4*. Hoboken, NJ: John Wiley & Sons; 2018.

44. Hauck C, Bach M, Hilbich C. A 4-phase model to quantify subsurface ice and water content in permafrost regions based on geophysical datasets. *Proceedings Ninth International Conference on Permafrost*, June 2008; 675–680.

45. Kane DL, Hinkel KM, Goering DJ, Hinzman LD, Outcalt SI. Nonconductive heat transfer associated with frozen soils. *Global Planet Change*. 2001;29(3–4):275-292.

46. ecoTech. TensioMark® [package insert]. Manual for installation and use of Tensiomarks 2014.

47. Blume HP, Brümmer GW, Fleige H, et al. Scheffer/Schachtschabel Soil Science. In: *1st ed.* 2016. Berlin, Germany: Springer; 2016.

48. Kujala K, Seppälä M, Holappa T. Physical properties of peat and palsa formation. *Cold Reg Sci Technol*. 2008;52(3):408-414.

49. Pellet C, Hilbich C, Marmy A, Hauck C. Soil moisture data for the validation of permafrost models using direct and indirect measurement approaches at three alpine sites. *Front Earth Sci*. 2016;3(91):1-21. https://doi.org/10.3389/feart.2015.00091

50. Rist A, Phillips M. First results of investigations on hydrothermal processes within the active layer above alpine permafrost in steep terrain. *Norsk Geografisk Tidsskrift-Norwegian J Geogr*. 2005;59(2):177-183.

51. Matsuoka N. Soil moisture variability in relation to diurnal frost heaving on Japanese high mountain slopes. *Permafr Periglac Process*. 1996;7(2):139-151.

52. Arnalds Ó. Dust sources and deposition of aeolian materials in Iceland. *Icel Agric Sci*. 2010;23:3-21.

53. Kneisel C, Hauck C. Electrical methods. In: Kneisel C, Hauck C, eds. *Applied Geophysics in Periglacial Environments. Cambridge*. Cambridge, UK: Cambridge University Press; 2008:3-27.

54. Loke MH, Acworth I. Dahlin T. A comparison of smooth and blocky inversion methods in 2D electrical imaging surveys. *Explor Geophys*. 2003;34(3):182-187.

55. Chambers J, Ogilvy R, Kuras O, Cripps J, Meldrum P. 3D electrical imaging of known targets at a controlled environmental test site. *Environ Geol*. 2002;41(6):690-704.

56. Sjödahl P, Dahlin T, Zhou B. 2.5 D resistivity modeling of embankment dams to assess influence from geometry and material properties. *Geophysics*. 2006;71(3):G107-G114.

57. Farbrot H, Etzelmüller B, Schuler TV, et al. Thermal characteristics and impact of climate change on mountain permafrost in Iceland. *J Geophys Res Earth Surf*. 2007;112(F3). https://doi.org/10.1029/2006JF000541

58. Ross N, Brabham PJ, Harris C, Christiansen HH. Internal structure of open system pingos, Adventdalen, Svalbard: the use of resistivity tomography to assess ground-ice conditions. *J Environ Eng Geophys*. 2007;12(1):113-126.

59. Campbell S, Affleck RT, Sinclair S. Ground-penetrating radar studies of permafrost, periglacial, and near-surface geology at McMurdo Station, Antarctica. *Cold Regions Sci Technol*. 2018;148:38-49.

60. Heincke B, Green AG, Kruk J, Horstmeyer H. Acquisition and processing strategies for 3D georadar surveying a region characterized by rugged topography. *Geophysics*. 2005;70(6):K53-K61.

61. Lambot S, André F, Slob E, Vereecken H. Effect of antenna-medium coupling in the analysis of ground-penetrating radar data. *Near Surf Geophys*. 2012;10(6):631-639.

62. Baker GS, Jordan TE, Pardy J. An introduction to ground penetrating radar (GPR). *Special Papers - Geol Soc am*. 2007;432:1-18.

63. Everett ME. Ground-penetrating radar. In: Everett ME, ed. *Near-Surface Applied Geophysics*. Cambridge, UK: Cambridge University Press; 2013:239-278.

64. Degenhardt JJ. Development of tongue-shaped and multilobate rock glaciers in alpine environments–Interpretations from ground penetrating radar surveys. *Geomorphology*. 2009;109(3–4):94-107.

65. Dusik JM, Leopold M, Heckmann T, et al. Influence of glacier advance on the development of the multipart Riffeltal rock glacier, Central Austrian Alps. *Earth Surf Process Land*. 2015;40(7):965-980.

66. Monnier S, Kinnard C. Internal structure and composition of a rock glacier in the Dry Andes, inferred from ground-penetrating radar data and its artefacts. *Permafr Periglac Process*. 2015;26(4):335-346.

67. Davis JL, Annan AP. Ground-penetrating radar for high-resolution mapping of soil and rock stratigraphy. *Geophys Prospect*. 1989;37(5):531-551.

68. Seppälä M. The origin of palsas. *Geogr Ann: Series A, Phys Geogr*. 1986;68(3):141-147.

69. Chamberlain EJ. *Frost susceptibility of soil, review of index tests*. Hanover, NH: Cold Regions Research and Engineering Lab; 1981.

70. Coultish T, Lewkowicz A. Palsa dynamics in a subarctic mountainous environment, Wolf Creek, Yukon Territory, Canada. *Proceedings of the 8th International Conference on Permafrost, Zurich, Switzerland*. 2003; 2125.

71. Marklund P. *A 2D Electrical Resistivity Survey of Palsas in Tavvavuoma, sub-arctic Sweden [MSc thesis]*. Uppsala, Sweden: University of Uppsala; 2014.

72. Seppälä M. Surface abrasion of palsas by wind action in Finnish Lapland. *Geomorphology*. 2003;52(1–2):141-148.